

Updated measurement method and uncertainty budget for direct emissivity measurements at UPV/EHU

I. González de Arrieta^a, T. Echániz^{b,*}, R. Fuente^b, J.M. Campillo-Robles^a,
J.M. Igartua^a, G.A. López^a

^a*Applied Physics II, University of the Basque Country UPV/EHU, Leioa, 48940, Spain*

^b*Applied Mathematics, University of the Basque Country UPV/EHU, Plaza Ingeniero
Torres Quevedo 1, Bilbao, 48013, Spain*

Abstract

This work reports on the upgrades made to the direct emissivity measurement facility of the UPV/EHU. The instrumental improvements consist of, among others, a high-vacuum system and wider temperature range (300 – 1273 K). Methodological developments include a refined measurement equation with updated parameters and a reworked ISO-compliant uncertainty budget, and a Monte Carlo procedure for accurate calculations of total emissivities from spectral data. These upgrades have been demonstrated and validated in measurements of both metallic and ceramic materials. The results obtained in this work are applicable to similar experimental devices for emissivity measurements in order to report reliable emissivity data.

Keywords: measurement uncertainty, emissivity, infrared, temperature measurement, radiometry, Monte Carlo

1. Introduction

Emissivity is an essential thermophysical property for a number of scientific and industrial applications, but the lack of well-established experimental procedures and reference materials complicates the comparison of data among different research groups. Relatively few attempts at intercomparisons have been pursued, mostly in recent years [1–5]. Some ASTM standards are available [6–11], but they do not correspond well to most research devices in operation, which are custom-made by research groups. It is well-known that uncertainty budgets can widely differ among research groups even for standardized techniques, especially for temperature-dependent properties [12]. In particular, the presence of systematic errors is troublesome and can only be reliably determined by intercomparisons with well-defined uncertainty budgets [13]. Furthermore, the development of new measurement methods, improved uncertainty calculations and characterization of reference materials have all been identified as key prospects of a recent European Roadmap of Thermophysical Properties [14]. Therefore, the development of credible uncertainty budgets and further efforts at standardizing emissivity measurements is a priority.

*Corresponding author

Email address: `telmo.echaniz@ehu.es` (T. Echániz)

There are many experimental devices capable of emissivity measurements, which vary in their methodology, calibration procedures, temperature measurement, and heating system, among others. A comprehensive review up to 2015 can be found in Ref. [15], while a remarkable amount of new instruments has been developed more recently [16–29]. The University of the Basque Country (UPV/EHU) has contributed to this goal with the HAIRL radiometer (High Accuracy Infrared Radiometer at Leioa), built from original designs [30] and referenced by some of the newly built instruments. As part of the efforts at improving the metrological quality of this radiometer, it has recently taken part in a Round Robin test for intercomparison of emissivity measuring devices [1]. However, some of its features required a significant update in order to be able to cope with new challenges. For example, emissivity measurements in near-room-temperature applications, such as photovoltaic cells, biomaterials, textiles or polymers, require a particularly careful estimation of the uncertainty budget [17, 31]. Furthermore, low-emitting materials (such as noble metals) have also been known to require more sensitive treatment of the uncertainty in order to bridge together the often conflicting results from different emissivity measurements setups [32, 33].

The standard practice for calculating uncertainty budgets is to follow the ISO *Guide to the Expression of Uncertainty in Measurement* (GUM) [34]. A previous uncertainty budget for the HAIRL radiometer based on such Guide is available in the literature [35]. However, important advances have been made ever since, which motivate an improved reference. Several sources of uncertainty were calculated in a non-GUM-compliant way, while systematic errors were not thoroughly discussed. Besides, only metallic materials were considered, whereas a more general treatment of the uncertainty would be desirable to deal with other materials. This is because the lack of reference materials is a significant obstacle in the improvement of the accuracy of radiometers. ARMCO iron was previously used as a reference material by this laboratory [36], but it is unsuitable for high-temperature measurements due to oxidation and the presence of a structural phase transition. This paper features results for a wider range of materials, including ceramics, which were not covered in the previous uncertainty budget. Their high emissivities also allow them to be measured at temperatures lower than those possible for metals in this setup (300 – 373 K). Finally, no discussion was given in the previous reference to directional or total emissivity measurements and their uncertainties.

In this paper, a review of the updated features and measurement methodology of the HAIRL radiometer, as well as a revised uncertainty budget, are elaborated. The uncertainty budget is deduced according to the principles expressed in the GUM and it is computed for representative materials covering a range of temperatures, emissivities and emission angles. Calculations of integrated total emissivities and their uncertainty propagation using a Monte Carlo method (as detailed in Supplement 1 to the GUM [37]), are also derived.

2. Experimental device

The experimental device used in these measurements is the HAIRL radiometer, which has been in use for more than 14 years and has been constantly updated [30]. It is based on a T-form geometrical configuration described schematically in Fig. 1. It consists of a Fourier-transform infrared spectrometer (FTIR),

Parameter	Range
Wavelength (λ , μm)	1.43 – 25
Viewing angle (θ , $^\circ$)	0 – 80
Temperature (T , K)	300 – 1273
Pressure (P , Pa)	$10^5 - 5 \cdot 10^{-3}$
Sample atmosphere	Air, Ar, $\text{N}_2 + \text{H}_2$

Table 1: List of updated standard parameters for emissivity measurements in the HAIRL radiometer.

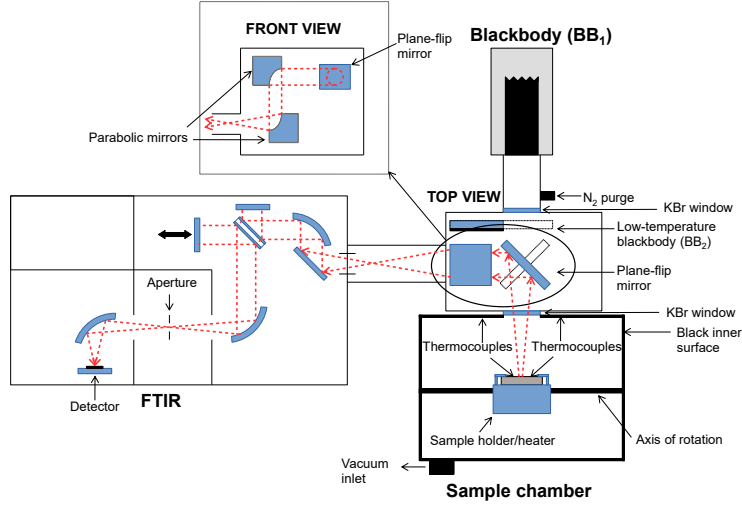


Figure 1: Schematic view of the HAIRL radiometer of the UPV/EHU. The four standalone parts are noted in bold letters, with the optical entrance being shown in both top and front views for better appreciation. The low-temperature blackbody plate is located inside the optical entrance.

a vacuum sample chamber, a reference blackbody (Isotech Pegasus R[®]) and an optical entrance box that allows switching between the blackbody source and the sample chamber by a rotating plane mirror. The updated technical parameters are listed in Table 1. Note that some of these ranges may not be applicable for all measurements.

The spectrometer is a Bruker IFS 66v/S[®] vacuum model. Its optical system consists of conventional KBr optics and a Ge/KBr beamsplitter, with the possibility of using two IR detectors: thermal DLaTGS (1.43 – 25 μm) and cooled quantum InGaAs (0.83 – 2.5 μm). The InGaAs detector will not be covered in this work as it has not been as thoroughly tested as the DLaTGS one. The FTIR has the optical entrance system attached directly to its source port, which means it is evacuated to the same degree. This system contains a plane switching mirror to select between the radiance coming from the sample chamber and that coming from the high-temperature blackbody source, as well as two parabolic mirrors to redirect this radiances to the focal point of the FTIR. The additional blackbody source is located inside the optical box, in the form of a steel shutter that has been coated with Nextel 811-21[®] black paint.

The sample chamber consists of a double-wall stainless steel structure, coated with Nextel 811-21[®] black paint to avoid multiple reflections of radiation inside

the chamber. A cooling system allows controlling the temperature by running water inside the double wall. The sample holder is located on top of a rotating axis to allow for directional measurements. The vacuum system which controls the sample atmosphere has been upgraded to a turbomolecular pump, which also allows for higher measurement temperatures for metals due to the reduced risk of oxidation. A Zr foil can be used as an oxygen getter for measurements on highly reacting materials, such as titanium or vanadium alloys [38].

The samples are heated from the back by a resistive wire, which was previously embedded inside two steel plates [30]. In this new version, a sample holder with direct radiative contact between sample and wire has been developed. This improves the thermal contact by avoiding thermal gradients across the base plate. The use of a more compact sample holder has allowed for higher measurement temperatures. The regular heating wire is made of Kanthal APM[®], a dispersion-strengthened FeCrAl alloy for use up to 1523 K; whereas a sintered quality Ta heating wire from Plansee (99.95% purity) can be used for vacuum measurements for temperatures above 1173 K. These improvements allow for sample surface temperatures up to 1273 K (as, for example, in a conductive BN ceramic [39]). This new upper temperature limit compares favourably to the previously stated limit of 1050 K in Ref. [30].

Typical sample sizes are disks of $\varnothing 60$ mm or rectangular samples of 40×20 mm² in a sample holder of $\varnothing 60$ mm. Typical thicknesses range from 0.5 mm to 3 mm, with thicker samples experiencing an excessive axial temperature gradient due to the back-heating configuration. Surface temperature is measured, when possible, by two Type K thermocouples, which are spot-welded to the surface 5 mm away from the center. Each wire is spot-welded independently onto the surface (intrinsic method) to minimize systematic mounting errors or contact spots away from the surface [40]. The wire diameter is 0.2 mm, in order not to excessively disturb the temperature distribution by heat conduction. Alternatively, the thermocouples can be mounted by drilling holes through the material and making mechanical contact at the surface. This method can be described as an intrinsic method with contact resistance [40]. Differences between the two mounting methods will be discussed in Section 4.2.1. For ceramic materials, which cannot be welded, an alternative radiometric temperature measurement method is performed, which will be discussed in Section 4.2.2.

The high-temperature blackbody employed is a commercial high-emissivity tubular furnace (Isotech Pegasus R[®]) with a diameter of $\varnothing 20$ mm, a depth of 65 mm, and a minimum certified emissivity of 0.995. It is made of graphite and features a diffuse surface and a bottom formed of 120° cones to deflect light from the aperture. Its temperature is controlled by a PID controller and measured with a calibrated Type R thermocouple embedded into the bottom of the tube below the textured surface. When measuring its radiance, it can be purged with N₂ gas. In contrast, the low-temperature reference is a steel disk painted with Nextel 811-21[®] black paint, acting as a greybody. Its temperature is measured by a Type K thermocouple.

3. Measurement and calibration method

3.1. Previous approach

The measurement method used at UPV/EHU is based on the *blacksur* method, which has been deemed the most accurate of the simplified direct radio-

metric methods [41]. This method models the sample chamber as a blackbody environment with a much larger area than both the IR window and the sample. The assumption of a large enclosure is the key approximation in this approach, since it simplifies the calculation of the radiation configuration factors and allows considering only a single reflection of a blackbody spectrum. Therefore, the radiance coming out of the chamber window can be described by a simple combination of the self-emitted sample radiation and the blackbody radiation from the enclosure reflected on the sample:

$$L^* = \varepsilon L_s + (1 - \varepsilon) L_{sur} \quad (1)$$

where L^* is the effective radiance, ε is the emissivity of the sample, L_s is the blackbody radiance of the sample, and L_{sur} is the blackbody radiance of the surroundings.

Assuming a linear instrumental response, typical of thermal detectors like DLaTGS, the following relation between the measured signal and the radiance coming from the sample can be formulated:

$$S_s = R A_s F_{s-det} L^* + S_0 \quad (2)$$

where S_s is the measured signal coming from the sample chamber, R stands for the response function of the FTIR, A_s for the sample emission area, F_{s-det} for the radiation geometric factor between the measured spot and the detector, and S_0 for the background radiation inside the spectrometer.

The instrument is required to be calibrated with blackbody sources. This procedure is performed by the modified two-temperature method, which has been discussed in the literature and compared satisfactorily to the more common multi-temperature and two-temperature approaches [42]. In this calibration method, two independent sources of blackbody radiation (a high-temperature source, bb_1 , and a room temperature one, bb_2) are used, which allows for a quicker calibration than by using the same source at two different temperatures. Some of the problems that have been noted for this type of approach [17] are mostly avoided by measuring the two blackbody sources at very different temperatures ($\Delta T \sim 800$ K) and keeping one of them near room temperature in order to properly account for the contribution of the background radiation S_0 [42].

The system of equations required for calibration is thus:

$$S_{bbi} = R A_{bbi} F_{bbi-det} \varepsilon_{bbi} L_{bbi} + S_0 \quad \text{for } i = 1, 2 \quad (3)$$

Since both radiance references are located along the same optical path, $A_{bb1} F_{bb1-det} = A_{bb2} F_{bb2-det}$ was assumed. If the observed areas and configuration factors corresponding to the sample and reference measurements also coincide, then the definition of the R factor can incorporate them through $R A_s F_{s-det} = R A_{bb1} F_{bb1-det} \equiv R^*$. Finally, the previously employed measurement equation for the *blacksur* method is obtained by combining Eqs. 1 to 3 [35]:

$$\varepsilon = \frac{S_s - S_0 - R^* L_{sur}}{R^* (L_s - L_{sur})} \quad (4)$$

On a final note, Eq. 4 is applicable only when there are no additional (parasitic) radiance signals different from S_0 that need to be filtered out. It has

been proved that this is only possible for off-normal emission angles, as additional contributions can arise if a reflecting sample is located perfectly parallel to the KBr window and the detector [43]. Therefore, measurements reported as normal emissivities actually correspond to directional measurements at an incidence angle of 10° .

3.2. New approach

Eq. 4 has been recently modified in order to account for additional measurement parameters and improve its reliability. Firstly, the possibility of an anisotropic response in the form factors of both sides of the optical entrance is taken into consideration by introducing an anisotropic response function $a(\lambda)$ to account for the chromatic aberration due to different focal points at the left and right sides of the optical entrance. This is assumed to stem from a combination of residual misalignments in the optical entrance and FTIR. This results in the configuration factors for the sample and the references not being equal ($F_{s-det} = aF_{bb-det}$, where a is a measurable optical anisotropy factor). Secondly, the emissivities of the blackbodies were not considered in the previous equation. The emissivity of the commercial high-temperature blackbody was assumed equal to 1, whereas the emissivity of the low-temperature blackbody source was the only parameter considered. Thirdly, the calibration parameters R and S_0 are correlated because they are the solutions to a system of two equations (Eq. 3). Therefore, their uncertainties cannot be considered separately, so it is more effective not to include them in the measurement equation. By considering explicitly the reference data (radiances and emissivities) in Eq. 4, a more reliable expression for the *blacksur* measurement method is obtained:

$$\varepsilon = \frac{\frac{(S_s/a - S_{bb1}) \cdot (\varepsilon_{bb1}L_{bb1} - \varepsilon_{bb2}L_{bb2})}{S_{bb1} - S_{bb2}} + \varepsilon_{bb1}L_{bb1} - L_{sur}}{L_s - L_{sur}} \quad (5)$$

This measurement equation can be simplified by defining a ratio quantity Q that includes all radiance measurements:

$$Q = \frac{S_s/a - S_{bb1}}{S_{bb1} - S_{bb2}} \quad (6)$$

It must be noted that all measured radiances S_i are signed functions, which can be positive or negative depending on the wavelength and temperature of the source. In particular, it is well established that the S_{bb2} contribution is negative at room temperature, as the detector emits more radiation when aiming at a cold surface than the one that it receives from it [42]. The ratio parameter Q now includes all relevant radiance measurements onto one single function, leaving all the others solely as functions of non-radiometric parameters.

The final measurement equation is:

$$\varepsilon = \frac{Q \cdot (\varepsilon_{bb1}L_{bb1} - \varepsilon_{bb2}L_{bb2}) + \varepsilon_{bb1}L_{bb1} - L_{sur}}{L_s - L_{sur}} \quad (7)$$

This equation bears strong resemblance to one used at Physikalisch-Technische Bundesanstalt (PTB, Berlin) for their in-air and vacuum emissivity measuring apparatuses [19, 44]. This formulation allows for separation of the sources of error in three uncorrelated sets of parameters: signals (Q), temperatures (T_s , T_{sur} , T_{bb1} , T_{bb2}), and emissivity of the references (ε_{bb1} , ε_{bb2}). The resulting parameters

Table 2: Uncertainty sources for emissivity measurements using the HAIRL radiometer and their respective subsources. Type A corresponds to statistical sources and Type B to non-statistical ones [34]. The standard uncertainties of quantities described by t -distributions are calculated following Section 6.4.9 of Ref. [37]. N.S.: not significant.

Source of uncertainty	Symbol	Type	Distribution
1) Signal ratio	Q		
Sample signal repeatability	S_s	A	Gaussian
Non-linearity of the FTIR		B	N.S.
Size-of-source effect		B	N.S.
High- T blackbody repeatability	S_{bb1}	A	Gaussian
Low- T blackbody signal repeatability	S_{bb2}	A	Gaussian
Optical anisotropy	a	B	N.S.
2) Sample temperature	T_s		
Metals			
Repeatability and inhomogeneity		A	t -distribution
Thermocouple (K) accuracy		B	Rectangular
Ceramics			
Inaccuracy of ε_{Chris}		A	Gaussian
Temperature dependence of ε_{Chris}		B	Gaussian
3) Surroundings temperature	T_{sur}		
Repeatability and inhomogeneity		A	t -distribution
Thermocouple (K) accuracy		B	Rectangular
Emissivity of the surroundings		B	N.S.
4) Blackbody references			
High-temperature blackbody temperature	T_{bb1}		
Temperature inhomogeneity		B	Gaussian
Thermocouple (R) accuracy		B	Gaussian
Low-temperature blackbody temperature	T_{bb2}		
Repeatability		A	Gaussian
Thermocouple (K) accuracy		B	Rectangular
High-temperature blackbody emissivity	ε_{bb1}	B	Rectangular
Nextel 811-21 emissivity	ε_{bb2}	B	Gaussian

are advantageous for uncertainty calculations, unlike those of the previous calibration (R and S_0). It should be reminded, however, that there is a correlation between the emissivity values at different wavelengths (i.e., $r(\varepsilon(\lambda_i), \varepsilon(\lambda_j)) \neq 0$), which will be important in the calculation of total emissivities in Section 5.

4. Sources of uncertainty in spectral measurements

The uncertainty budget of the *blacksur* method was first introduced in Ref. [35] and will be revised in this section, according to the new measurement equation (Eq. 7), and the new estimations of uncertainty for the base input quantities. It is based on the linearized GUM framework [34], considering only first-order uncorrelated terms. Two types of uncertainties are considered in this framework: Type A stands for statistical sources of error (accessible through repeated sampling and averaging), whereas Type B stands for non-statistical

sources (arising from non-experimentally accessible sources of information, such as calibration reports). A summary of the findings of this Section can be found in the uncertainty budget shown in Table 2. The sensitivity factors are obtained by partial derivation of Eq. 7:

$$\frac{\partial \varepsilon}{\partial Q} = \frac{\varepsilon_{bb1}L_{bb1} - \varepsilon_{bb2}L_{bb2}}{L_s - L_{sur}} \quad (8)$$

$$\frac{\partial \varepsilon}{\partial L_s} = \frac{L_{sur} - \varepsilon_{bb1}L_{bb1} - Q \cdot (\varepsilon_{bb1}L_{bb1} - \varepsilon_{bb2}L_{bb2})}{(L_s - L_{sur})^2} \quad (9)$$

$$\frac{\partial \varepsilon}{\partial L_{bb1}} = \frac{\varepsilon_{bb1}(1 + Q)}{L_s - L_{sur}} \quad (10)$$

$$\frac{\partial \varepsilon}{\partial L_{bb2}} = -\frac{\varepsilon_{bb2}Q}{L_s - L_{sur}} \quad (11)$$

$$\frac{\partial \varepsilon}{\partial L_{sur}} = \frac{\varepsilon_{bb1}L_{bb1} + Q(\varepsilon_{bb1}L_{bb1} - \varepsilon_{bb2}L_{bb2}) - L_s}{(L_s - L_{sur})^2} \quad (12)$$

$$\frac{\partial \varepsilon}{\partial \varepsilon_{bb1}} = \frac{L_{bb1}(1 + Q)}{L_s - L_{sur}} \quad (13)$$

$$\frac{\partial \varepsilon}{\partial \varepsilon_{bb2}} = -\frac{QL_{bb2}}{L_s - L_{sur}} \quad (14)$$

It should also be borne in mind that, in the case of the L_i radiances, the real uncertainties correspond to the temperature measurements T_i , and so it is necessary to introduce derivatives on Planck's law [45]:

$$L(\lambda, T) = \frac{2\pi C_1}{\lambda^5 (e^{C_2/\lambda T} - 1)} \quad (15)$$

where $C_1 = hc^2$ and $C_2 = hc/k_B$ are the first and second radiation constants, formed from fundamental constants.

The partial derivative with temperature then follows as:

$$\frac{\partial L_i}{\partial T_i} = \frac{2\pi C_1 C_2 e^{C_2/\lambda T_i}}{\lambda^6 T_i^2 (e^{C_2/\lambda T_i} - 1)^2} = \frac{L_i}{\lambda T_i^2} \frac{C_2 e^{C_2/\lambda T_i}}{(e^{C_2/\lambda T_i} - 1)} \quad (16)$$

Therefore, the final expression for the combined standard uncertainty u_c is:

$$\begin{aligned} u_c^2(\varepsilon) = & \left(\frac{\partial \varepsilon}{\partial Q} \right)^2 u^2(Q) + \sum_{i=1}^4 \left(\frac{\partial \varepsilon}{\partial L_i} \frac{\partial L_i}{\partial T_i} \right)^2 u^2(T_i) \\ & + \sum_{i=1}^2 \left(\frac{\partial \varepsilon}{\partial \varepsilon_{bbi}} \right)^2 u^2(\varepsilon_{bbi}) \end{aligned} \quad (17)$$

4.1. Signal ratio measurement

Repeatability in the measurement of the emitted radiances is one of the clearest sources of uncertainty in emissivity measurements, particularly for low-emitting samples or at low temperatures and short wavelengths. This is evaluated as a Type A uncertainty, that is, arising from a statistical analysis of Eq. 6:

$$u^2(Q) = \sum_{i=1}^3 \left(\frac{\partial Q}{\partial S_i} \right)^2 u^2(S_i) \quad (18)$$

where the uncertainty of the anisotropy factor a is neglected, and all three radiance measurements are described by uncorrelated Gaussian distributions corresponding to Type A uncertainties [34].

The uncertainty corresponding to the anisotropy a factor is routinely checked, especially during routine maintenance of the FTIR, by measuring the radiance emitted by an infrared source located at each side of the optical entrance. The result of the latest calibration is shown in Fig. 2. The standard uncertainty is calculated as a Type A uncertainty of 30 scans for each side of the entrance (sample and references). The uncertainty was larger at both ends of the spectrum due to lower radiances taking place at such wavelengths. The factor has been fitted to the simplest functional form that can replicate it:

$$a = \frac{S_R}{S_L} = m_1 + \frac{m_2}{\lambda^2} \quad (19)$$

where S_R and S_L stand for the measured calibration signals from the right (sample) and left (blackbody) compartments. The resulting parameters were found to be $m_1 = 0.99859 \pm 0.00003$ and $m_2 = -0.0472 \pm 0.0001$.

Practical reasons do not allow for frequent recalibrations of this parameter, so it is considered as a Type B uncertainty source. However, the quality of the fitting is such that it is deemed negligible in this uncertainty budget (assuming frequent recalibrations). Nevertheless, it should be kept in mind that it is a potential source of systematic errors. It is particularly important for very low or very high emitting materials, for which a drift in this value can lead to non-physical values of the emissivity (either negative or over 1).

Other sources can contribute to the radiance factor uncertainty. Non-linearity of the FTIR spectrometer with a thermal DLaTGS detector has been checked by a multi-temperature calibration procedure [17]. It stays below 0.2% in the $2 - 22 \mu\text{m}$ spectral range, with larger values outside that range. In the case of the size-of-source effect, the size of the blackbody aperture is $\varnothing 20 \text{ mm}$ and that of the usual samples is greater than $\varnothing 20 \text{ mm}$, while the measuring spot corresponding to the standard aperture size is estimated as $\varnothing 3.6 \text{ mm}$. It has been shown by other researchers that this effect can generally be neglected in emissivity measurements if both radiation source apertures are much larger than the measuring spot size [31, 46].

4.2. Sample temperature measurement

When considering the standard uncertainty of the temperature measurements in this experimental setting, two cases will be discussed: contact measurements with thermocouples for metals and non-contact pyrometric measurements using the Christiansen wavelength for ceramics [47]. The former was first

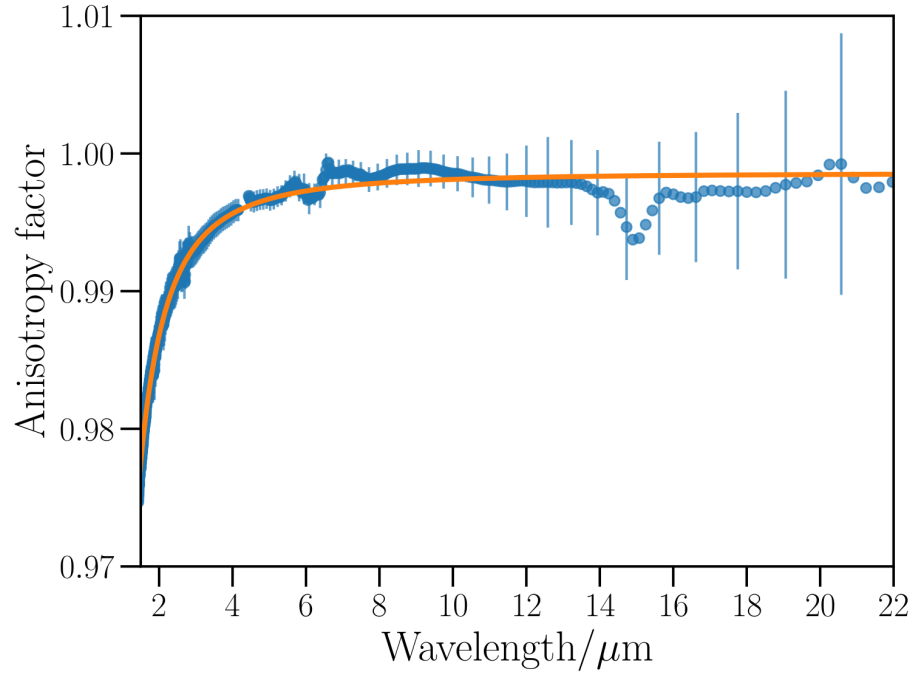


Figure 2: Experimentally determined anisotropy factor (a) and theoretical fit. Error bars correspond to the standard uncertainty ($k = 1$). The uncertainty of the fit is deemed negligible for all purposes. Note that the features around 6 and 15 μm correspond to residual absorption by water and CO_2 .

introduced in the previous uncertainty budget [35], whereas the latter has not yet been examined in our laboratory.

4.2.1. Metals (thermocouples)

There are three main sources of uncertainty when measuring temperatures with thermocouples that will be discussed in this section. The first source, of Type B, corresponds to the intrinsic accuracy of the sensors (Type K thermocouples). The second and third ones, of Type A, concern the temporal and spatial thermal inhomogeneity of the measured spot.

Regarding the accuracy of a standard Type K thermocouple, the corresponding ANSI C96.1 standard defines its limits of error as 0.75% of the temperature in °C or 2.2 K, whichever is greater [48]. In the past uncertainty budget by this group, this was quoted as the standard uncertainty of the temperature measurement [35]. However, this statement is part of the definition of the probe, as a thermocouple with lesser accuracy is no longer Type K [48]. Therefore, the standard uncertainty of this measurement must be estimated from the information available. Some groups have considered these limits of error as equivalent to a near-total 99.7% certainty with a coverage factor of $k = 3$ [48], while others have taken these limits as $k = 2$ [49]. In this work, a rectangular distribution has been taken, as recommended by the GUM when only an upper and a lower bound are available [34]. By assuming this distribution, the standard uncertainty of this source becomes $1/\sqrt{3}$ of either limit of error, whichever is greater:

$$u(T) = \frac{1}{\sqrt{3}} \cdot \begin{cases} 0.0075(T - 273.15) \\ 2.2 \text{ K} \end{cases} \quad (20)$$

Regarding the last two sources, they are estimated based on the differences between the readings of both thermocouples, located symmetrically across the measuring spot. For each temperature, a starting and ending temperature for each thermocouple are recorded, which leads to four temperature datapoints per measurement. Thus, the inhomogeneities may be described as a t -distribution with a number of degrees of freedom $\nu = 4 - 1$. Spatial and temporal inhomogeneities are treated equally, as they often arise from the same sources. Taking a Bayesian approach (as described in Section 6.4.9 of the Supplement 1 to the GUM [37]), it is possible to define an enlarged standard uncertainty for measurements characterized by the t -distribution:

$$u(x) = \left(\frac{n-1}{n-3} \right)^{1/2} \frac{s}{\sqrt{n}} \quad (21)$$

where n is the number of measurements (in this case, $n = 4$), and $s = \sqrt{\sum (x_i - \bar{x})^2 / (n - 1)}$ is the standard deviation.

The use of Eq. 21 simplifies the calculation of the uncertainty by avoiding the need to take the number of degrees of freedom into account [37]. Therefore, the resulting temperature is measured using four measurements of the type $T_i = \alpha + t_i$, where α is the systematic uncertainty, with a mean value equal to 0 and a standard uncertainty given by Eq. 20. The corresponding mean and standard uncertainty are thus given by:

$$\bar{T} = \frac{1}{n} \sum (\alpha + t_i) \equiv \frac{1}{n} \sum t_i \quad (22)$$

$$u^2(\overline{T}) = u^2(\alpha) + \left(\frac{n-1}{n-3}\right) \frac{s^2(t_i)}{n} \quad (23)$$

where $u(\alpha)$ is given by Eq. 20.

It should be borne in mind that the uncertainty of the α systematic effect may often not correspond exactly to that defined by Eq. 20. The main problem observed with Type K thermocouples is the potential effect of systematic deviations arising from problems such as short-range ordering and selective oxidation of the Chromel leg. Both issues lead to underestimations of the surface temperature, which induce overestimated emissivity values. An extensive literature on the biases and problems associated with Type K thermocouples has been produced [50–54]. Therefore, an upgrade to a Type N thermocouple is projected for the HAIRL to avoid these systematic errors.

As a final note, the equivalence of both methods for mounting thermocouples mentioned in Section 2 has been tested for an ARMCO iron sample in an Ar atmosphere for the usual stabilization time (20 minutes). The differences between the intrinsic welded and intrinsic pressed methods can be seen in Fig. 3. Both curves agree within less than the standard uncertainty for most temperatures, with no clear temperature dependence. The magnitude of this effect is reduced in vacuum due to the absence of convection effects. This systematic error arises from an imperfect thermal contact in the mechanical method, but it is not considered in the final uncertainty budget, as it is difficult to estimate for each material and application. Both methods lead to the same temperatures in the infinite-time limit [40], which means that the mechanical method is a suitable alternative given larger stabilization times compared to the welded method. Accordingly, systematic uncertainties arising from mounting errors are considered as the main source of uncertainty in high-temperature transient measurements [48]. This can contribute to an additional uncertainty source when using this method at the highest temperatures possible with this setup (~ 1273 K).

4.2.2. Ceramics (non-contact measurement)

Temperature measurements in ceramic materials are difficult to accomplish with contact temperature sensors because of their low thermal and electrical conductivities. Therefore, a non-contact temperature measurement method is desired, although the effect of the emissivity complicates this procedure. Fortunately, some ionic compounds have a well-defined wavelength at which the emissivity is close to 1 and is only very weakly dependent on temperature. This wavelength is known as the Christiansen point and has been used as a reliable method of measuring the surface temperatures of the ceramic materials that feature it [47]. Temperature measurements using the Christiansen wavelength are very useful because they are performed at the same time as the sample radiance measurements and largely avoid systematic errors due to thermal gradients, since the temperature is directly measured on the measuring spot itself. On the contrary, no widely recognized estimation of its uncertainty is available at the moment.

As in the case of metals, temperature measurements using the Christiansen method feature several sources of uncertainty. One of the most important ones concerns the determination of the emissivity of the Christiansen point itself, which depends on the accuracy of the method used to characterize it. The

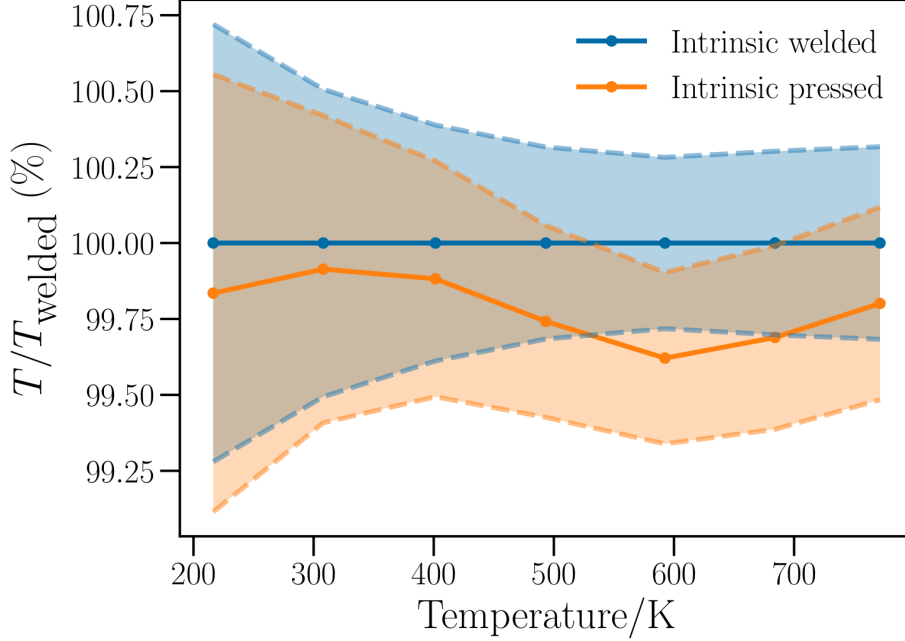


Figure 3: Study of the systematic error in temperature measurement by thermocouples drilled and pressed into the sample when compared to those spot-welded onto the surface for an ARMCO iron disk in Ar atmosphere. Shaded areas lines correspond to the relative standard uncertainties of both methods at each temperature.

relation between the emissivity and temperature uncertainties in this type of measurement is given by derivation of an approximation to Planck's law [55]:

$$\frac{u(T)}{T} = \frac{\lambda_{Chris} T}{C_2} \frac{u(\varepsilon_{Chris})}{\varepsilon_{Chris}} \quad (24)$$

where C_2 is the second radiation constant, and λ_{Chris} and ε_{Chris} are the parameters characterizing the Christiansen point at which the temperature is measured.

It is clear that the relative uncertainty of the measured temperature increases with the temperature itself, given a constant relative emissivity uncertainty. In this work, the Christiansen point is determined at room temperature using an Infragold-coated Bruker A 562-G integrating sphere (incidence angle 13° , 75 mm diameter) in the same FTIR as the high-temperature emissivity measurements. The sample is located in a port capable of measuring total (i.e., diffuse + specular) directional-hemispherical reflectance and the light source is a standard Globar source. The reflectivity can be traced to an absolute value by comparison to the Infragold standard. The standard uncertainty of this measurement is calculated as arising from Type A uncertainties in the measurement of the sample and reference reflected signals. Other sources of uncertainty, such as stray-light and non-linearity of the detector, have been deemed to be negligible. Geometric equivalence of the sample and reference ports is checked by comparing two identical references in both the reference and the sample ports.

The temperature uncertainty arising from the uncertainty in the emissivity at room temperature sets a lower bound to the overall uncertainty of the

Christiansen method. In particular, possible temperature dependences of the Christiansen point may affect the results more significantly. It is not possible at the moment to measure this property independently as a function of temperature. Therefore, the uncertainty arising from this source has to be estimated as an upper bound from literature data.

An error of ± 10 K in the determination of the melting point of single-crystal α - Al_2O_3 has been determined in a similar setup during emissivity measurements, which allows an estimation of $u(T_{\text{Chris}}) \sim 0.5\%$ at very high temperatures ($T \geq 2000$ K) [28]. Similar relative errors (0.1 – 0.7%) were reported in a comparison between the Christiansen wavelength method and a more complete one based on thermal flux balances and knowledge of the thermophysical properties of polycrystalline α - Al_2O_3 [18]. It should be noted that model-based temperature measurement methods can in fact be less accurate than radiometric ones under certain circumstances, as they strongly depend on the accuracy of numerous input parameters [55]. These results serve to validate the use of the Christiansen wavelength as a useful alternative to more complex measurement methods, with the added advantage of measuring the local temperature of the central spot, without radial gradients. Such a comparison to a thermal-flux based method has not been performed in our laboratory because the heating system employed does not allow a straightforward heat conduction modelling. Therefore, the uncertainty of the Christiansen method is estimated in this work as the average between the lower bound given by Eq. 24 and a 0.5% upper bound.

4.3. Surroundings temperature measurement

The treatment of the uncertainties arising from the chamber walls emission is similar to that of the sample temperature. It is treated as a blackbody ($\varepsilon = 1$) around room temperature, with its temperature measured by Type K thermocouples in two spots in the chamber walls which are symmetric with respect to the optical path of the measurement. As the temperature is less than 300 K (due to the water cooling system), the uncertainty of the thermocouples (Eq. 20) is taken as $2.2/\sqrt{3}$ K. The inhomogeneity of the enclosure temperature is calculated as that of the sample temperature; i.e., as a Type A uncertainty corresponding to four thermocouple measurements at two times and two locations. A Bayesian Type A uncertainty for small number of observations is again formulated, resulting in the same expression as Eq. 23.

Due to the use of a water cooling system, the average enclosure temperature is $\simeq 285$ K, instead of 298 K (the value assumed in the previous uncertainty budget [35]). The effect of the reduction in enclosure temperature is negligible at high sample temperatures, but makes precise measurements possible below 330 K. This is due to the fact that the greatest limitation of the *blacksur* method is that the emissivity diverges when the temperature of the sample and the surroundings are very close (see the denominator in Eq. 4). Finally, another possible source of uncertainty for this radiance is the assumption that the sample surroundings behave as a blackbody, whereas the emissivity of the coating employed has been measured to be closer to 0.97 [56]. However, it has been proved that the *blacksur* method differs less than 0.05% from the most accurate method (multi-reflections) when the emissivity of the chamber walls is greater than 0.95, provided that the sample chamber area is much larger than the spot size [41]. We therefore neglect the influence of this source of uncertainty.

4.4. Blackbody references

The measurement method requires radiance measurements of a high-temperature blackbody and a room-temperature Nextel 811-21[®] coating. The uncertainty of the measured signals has already been taken into account in the calculation of the Q ratio. The emissivities of the sources are $\varepsilon_{bb1} > 0.995$ for the conventional blackbody source (as specified by the manufacturer), and a spectral average of $\varepsilon_{bb2} = 0.97$ (with a standard uncertainty of 0.01) for the Nextel 811-21[®] coating, as calculated from literature data [56]. Not having any additional information on the uncertainty of the emissivity of the high-temperature blackbody, we consider only the uncertainty given by the certificate, modelled as a rectangular probability distribution function (PDF) with limits $0.995 < \varepsilon_{bb1} < 1$. Both uncertainties were neglected in the previous uncertainty budget [35], but will be considered in this updated version. In the case of the reference temperatures, their uncertainties are taken as the combination of a 0.3 K lack of spatial uniformity for the blackbody distribution of temperatures and 2 K for the calibration certificate of the high-temperature blackbody (measured with a Type R thermocouple), and $2.2/\sqrt{3}$ K for the low-temperature blackbody (Type K thermocouple, Eq. 20).

Finally, it should be noted that all two-temperature methods are susceptible of systematic errors. Two-temperature methods have been claimed to incur in significant errors in the determination of the internal radiation sources [17]. This can be crucial for certain measurements with low signals (low-emitting materials or room-temperature measurements). In the case of this radiometer, its calibration accuracy has been checked to be satisfactory given large enough (≥ 800 K) thermal differences between both blackbody references, with one of them required to stay at room temperature to properly account for the aforementioned internal radiation sources [42]. This contrasts with the approach followed by PTB, among others, who choose blackbody references which have the most similar radiation temperature to the sample [19]. In both cases, two-temperature methods are considered to be suitable given a linear detector, such as DLaTGS, and sufficiently good control of the blackbody temperatures and the spectrometer drift.

4.5. Combined standard uncertainty of representative materials

The uncertainty budget described above for spectral emissivity measurements is applied in this subsection to two materials, a metal and a ceramic. Nickel was chosen as the metallic example based on previous experience with this material [57]. A sputtering target synthesized using the Mond process with a diameter of 50 mm and a thickness of 3.2 mm was used. Its nominal purity was $> 99.99\%$, with 15 ppm Fe and 10 ppm S as the main impurities. It was mechanically polished with alumina powder to an average surface roughness of $R_a = 0.03 \mu\text{m}$ and a root-mean-square value of $R_q = 0.04 \mu\text{m}$, as measured with a mechanical profilometer (Mitutoyo SJ201). Its emissivity and standard uncertainty are shown in Fig. 4. The uncertainty tendencies can be more easily appreciated as relative uncertainties in Fig. 5. It can be seen that the uncertainty is very large at 473 K for all wavelengths, and quickly drops with temperature. Regarding its wavelength dependence, it tends to increase with wavelength for all temperatures, except at short wavelengths and low temperatures, where it can also reach large values. It is interesting to note that the

previous uncertainty budget reported generally greater uncertainties at shorter rather than larger wavelengths [35].

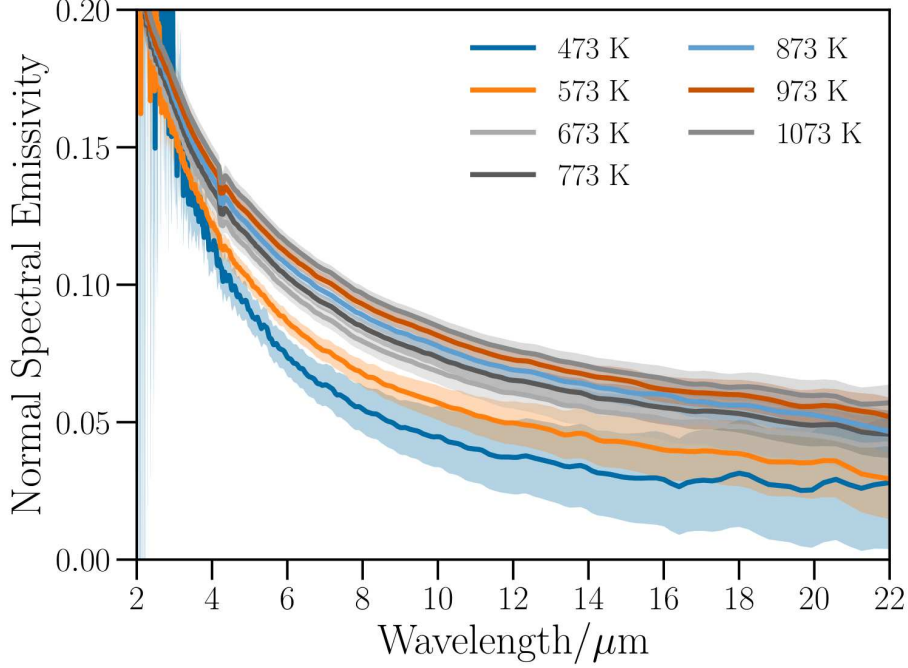


Figure 4: Normal spectral emissivity of Ni as a function of temperature. Shaded regions correspond to standard uncertainties ($k = 1$).

In the case of ceramic materials, a 0.43 mm-thick single crystal of Al_2O_3 has been chosen. It is oriented perpendicular to the c axis with a 0.2° misorientation angle. It was epi-polished on one side to a roughness of $R_a < 0.3$ nm. It was synthesized by the Czochralski method, with a purity of $> 99.99\%$. Due to its semi-transparency at shorter wavelengths, it was measured using a low-emissivity iron substrate in order to reduce the spurious radiation from the highly-emitting heating plate in the back. The resulting spectra are satisfactory down to a wavelength of $4 \mu\text{m}$. The temperature was measured assuming an emissivity at the Christiansen wavelength of 0.989 , as measured at room temperature (with an uncertainty of 0.002). The measurements and the relative standard uncertainties can be seen in Figs. 6 and 7. It is clear that the relative uncertainties at higher temperatures are much lower than those of nickel, mainly due to the higher emissivity values. This shows that, for most of the mid-infrared range, the lowest relative uncertainties achievable using the HAIRL radiometer are $1 - 2\%$. Nevertheless, the relative uncertainty at low temperatures is significant, particularly in the low-emissivity regions at long wavelengths.

These results on sapphire demonstrate the capability of the apparatus to measure the emissivity of ceramic materials, as well as dealing accurate emissivity values at relatively low temperatures even for emissivity values of 0.2 or below. This point is further illustrated by a comparison between this direct method and an indirect one using an integrating sphere at room temperature (Fig. 8). There is a good agreement between both methods in the region in

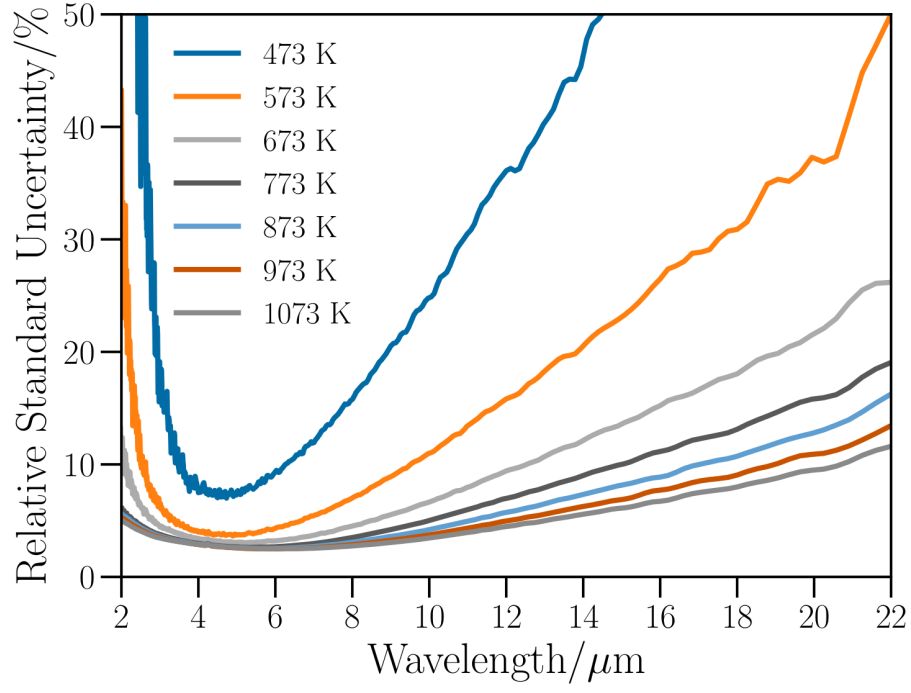


Figure 5: Relative standard uncertainties ($k = 1$) of the normal spectral emissivity measurements of Ni.

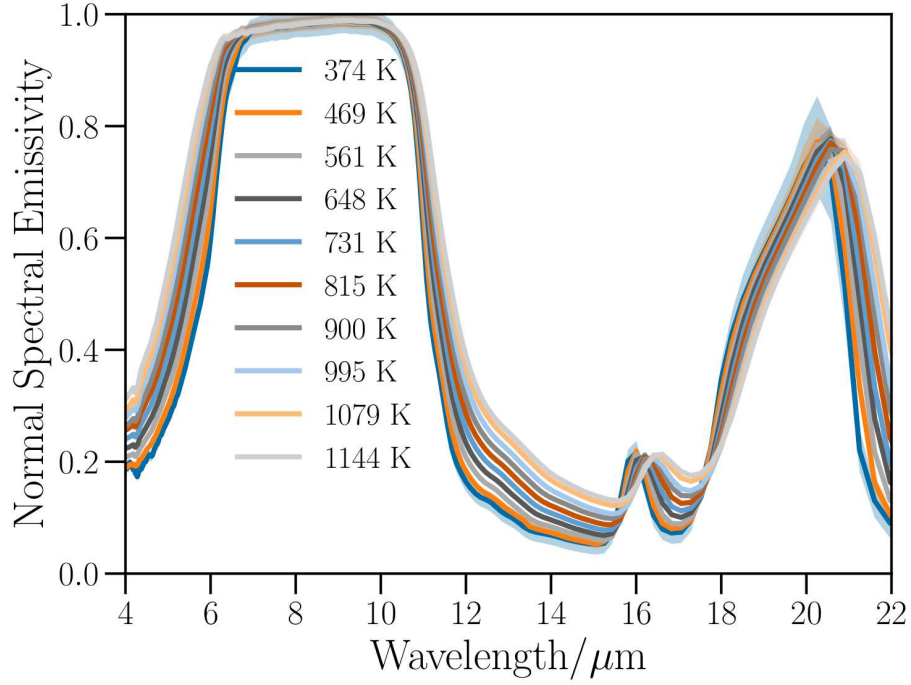


Figure 6: Normal spectral emissivity of sapphire (single-crystal Al_2O_3) as a function of temperature. Shaded regions correspond to standard uncertainties ($k = 1$).

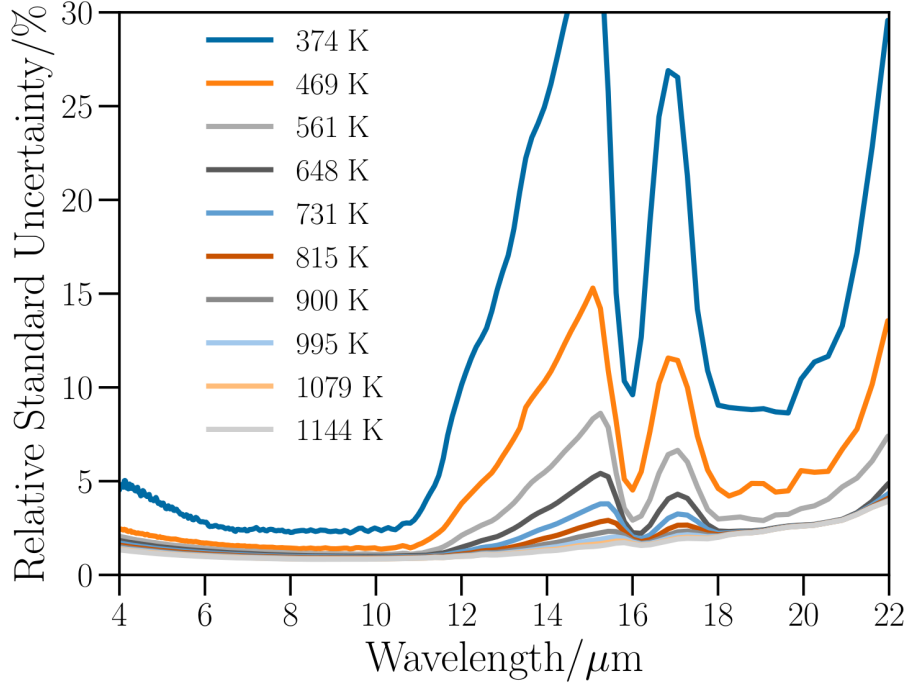


Figure 7: Relative standard uncertainties ($k = 1$) of the normal spectral emissivity measurements of sapphire Al_2O_3 .

which the material is completely opaque and equivalence between ε and $1 - \rho$ is expected [45].

As can be seen in Figure 6, the standard uncertainty for ceramic materials is low for most wavelengths. This stems from the greater signal-to-noise ratio of high-emissivity materials, as well as the reduced contribution by other radiance sources (surroundings, detector). Nevertheless, these measurements were performed at 373 K, almost 200 K less than the lowest temperature considered in the previous uncertainty budget [35]. Emissivity measurements at such low temperatures are easier for high-emitting ceramics than for metals. The temperature can be reduced even further in the case of highly emitting materials, given that the calibration procedure is accurate enough and that the temperature of the vacuum chamber and the sample are sufficiently different. The latter is the main drawback of the *blacksur* method, which has a divergence in the denominator (Eq. 4) when those two temperatures become equal [41].

The relative contributions of each uncertainty source for both materials are shown in Figs. 9 and 10. Some commonalities can be appreciated. For example, for both materials there is a general increase with temperature of the relative importance of the the uncertainties corresponding to the sample temperature and the high-temperature bb_1 source temperature and emissivity uncertainties, whereas those corresponding to the low-temperature bb_2 source and the surroundings temperature decrease. This is expected, as these latter sources of uncertainty correspond to low-temperature radiance sources, the influence of which is greatly reduced when the emission from the sample is increased at

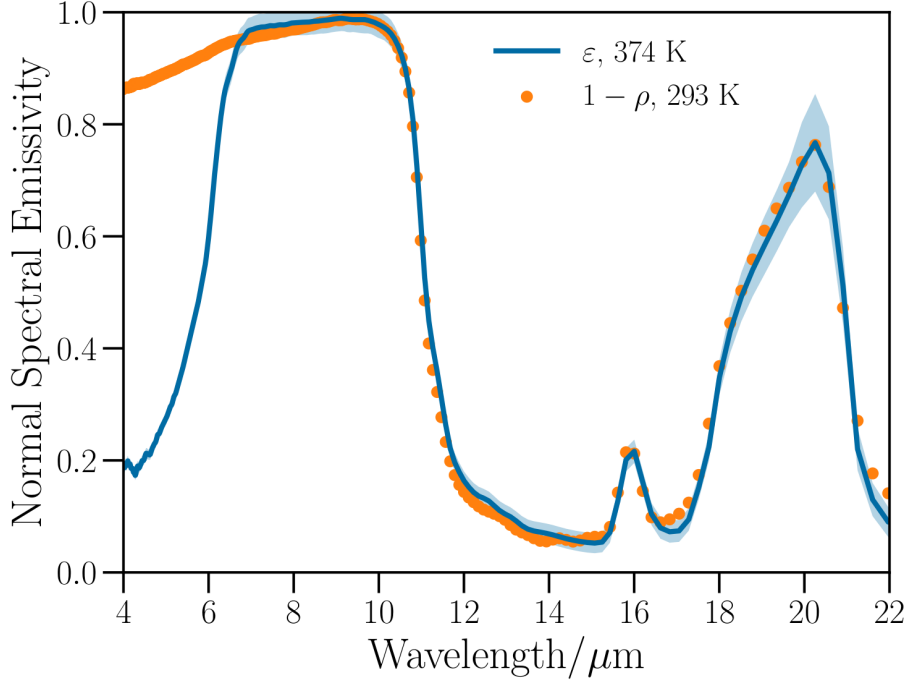


Figure 8: Normal spectral emissivity of sapphire Al_2O_3 measured directly with the HAIRL radiometer at 374 K and in an indirect mode with an integrating sphere at room temperature.

higher temperatures. Nevertheless, some influence of them can still be observed at long wavelengths for the highest temperatures, especially for Ni. On the contrary, the sample temperature uncertainty increases with temperature for both materials and is enhanced at shorter wavelengths, which makes it the dominant source in that spectral range and medium-to-high temperatures. Also, the influence of the high-temperature blackbody becomes larger for both materials as their radiances approach those of that reference source.

Some differences in the relative weights for each material can also be distinguished. At low temperatures and short wavelengths, the uncertainty of Ni is dominated by the radiance uncertainty, due to the very low signal reaching the detector from this low-emissivity sample. On the contrary, this uncertainty is larger for sapphire at longer wavelengths. It is at the lower temperatures where the uncertainty sources of both materials differ the most, although the general trends still hold.

5. Calculation and propagation of uncertainties of integrated quantities

5.1. Integration of spectral data

The sections above have dealt with measurements of the spectral directional emissivity. This parameter depends not only on temperature, but also on wavelength and emission angle; whereas, for most heat transfer applications, details on such dependences are often irrelevant. It is for this reason that integrated

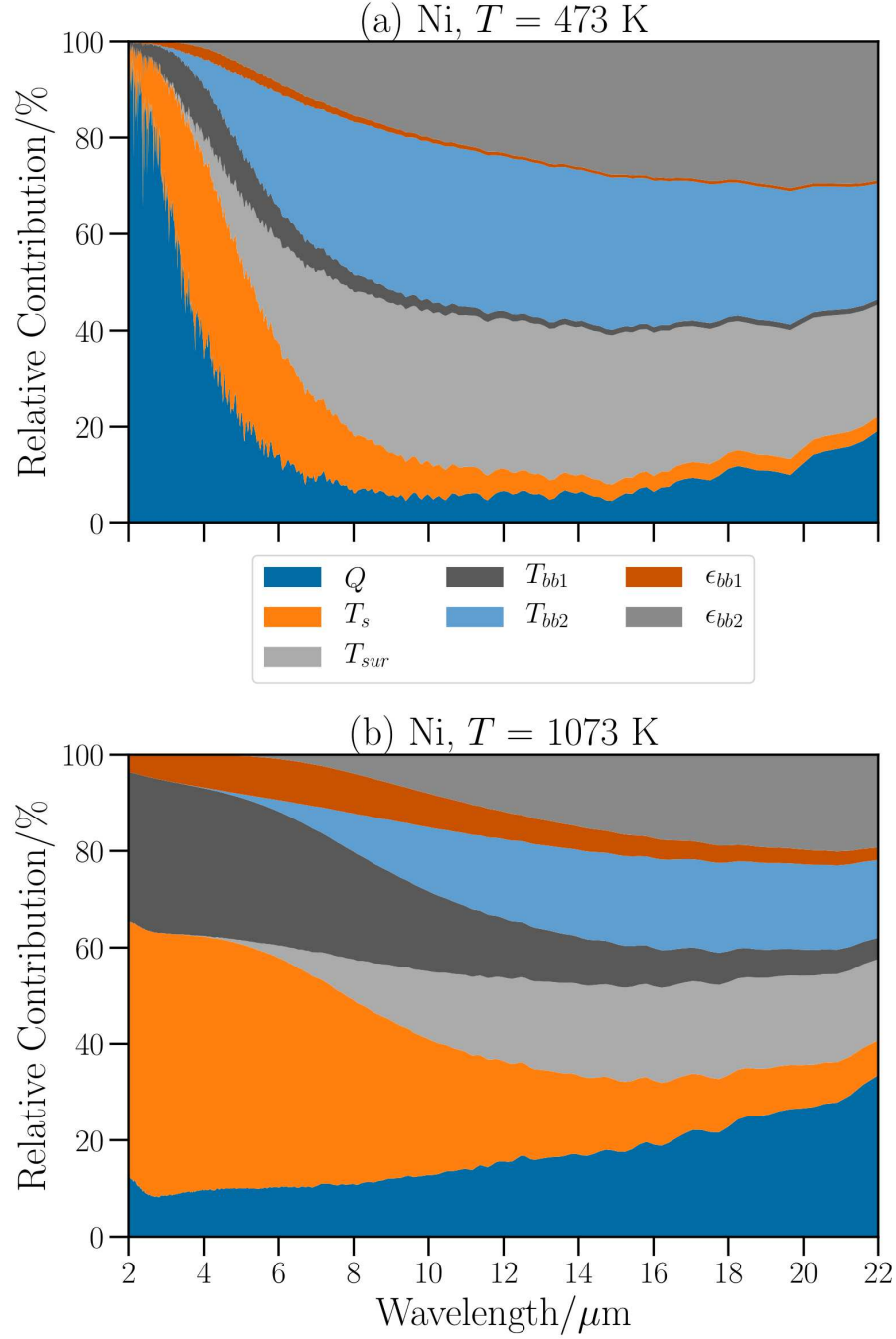


Figure 9: Relative standard uncertainties of the normal spectral emissivity of Ni at the lowest (a) and highest (b) temperatures measured.

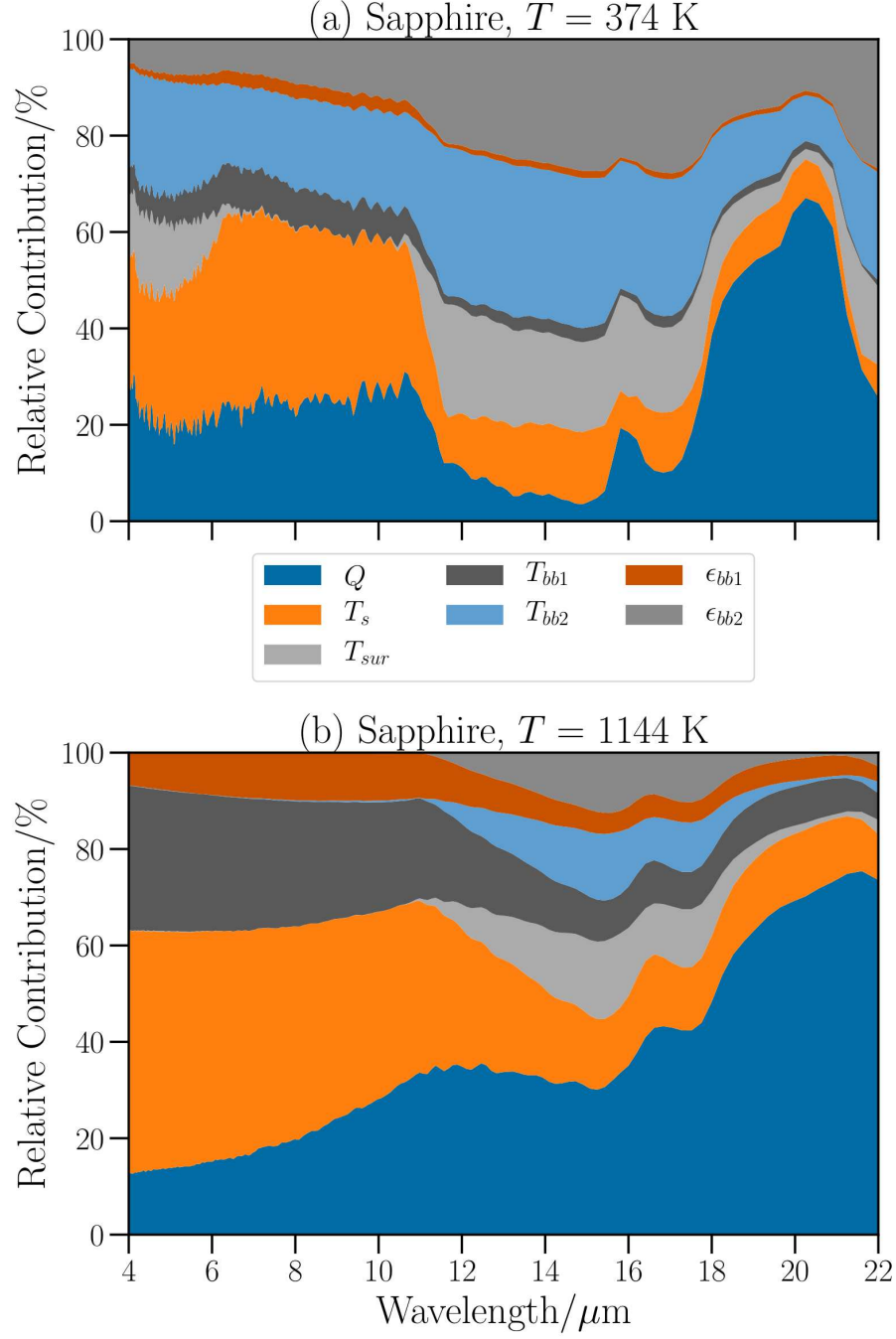


Figure 10: Relative standard uncertainties of the normal spectral emissivity of sapphire at the lowest (a) and highest (b) temperatures measured. Note that the spectral range is restricted to 4 – 22 μm .

quantities, such as the total normal or total hemispherical emissivities, are often more useful for engineering applications. These quantities can be measured by radiometric or calorimetric methods, which rely on very different approaches but have been shown to be equivalent [58]. For radiometric methods, such as the one described in this work, the total directional emissivity (of which the total normal is a special case) and the total hemispherical emissivity are defined from their spectral counterparts as follows [45]:

$$\varepsilon_T(\theta, T) = \frac{\int_0^\infty \varepsilon(\lambda, \theta, T) L(\lambda, T) d\lambda}{\int_0^\infty L(\lambda, T) d\lambda} \quad (25)$$

$$\begin{aligned} \varepsilon_H(T) &= \frac{1}{\pi} \int_0^{2\pi} d\phi \int_0^{\pi/2} \varepsilon_T(\theta, T) \cos(\theta) \sin(\theta) d\theta \\ &\equiv \int_0^{\pi/2} \varepsilon_T(\theta, T) \sin(2\theta) d\theta \end{aligned} \quad (26)$$

where θ is the polar angle and ϕ is the azimuthal angle, which is assumed to bear no influence [45].

A common problem of radiometric methods is the difficulty of measuring the entire spectral range in which thermal radiation may be emitted (i.e., from the far-infrared to the visible range). A method for calculating the total normal emissivity of metallic materials from directional spectral measurements in a restricted spectral range was introduced in Ref. [59]. This method involved calculating the total normal emissivity through a numerical integration of the available spectral data and two possible extrapolations, an overestimation and an underestimation. Therefore, the best estimate was found to be the average of the values obtained using each of the two extrapolation procedures, with the uncertainty being the difference between them. Based on the general knowledge that the wavelength dependence of the emissivity of metals is monotonic throughout the infrared range [45], this extrapolation procedures assumes that the possible values are contained within the last measured data point at each end and the physical limit of the emissivity (either 0 or 1).

This method approaches the correct value of the total emissivity given a sufficiently wide spectral range without requiring actual information of the emissivity in the extrapolated region. This can be regarded as an application of the principle of maximum entropy, as described in the GUM [34].

The maximum-entropy probability distribution for extrapolations of the spectral emissivity to the full electromagnetic spectrum when the available data is restricted to a spectral range $[\lambda_1, \lambda_2]$, and the emissivity is known to be monotonically decreasing with wavelength, is given by:

$$\varepsilon_T = \frac{\pi}{\sigma T^4} \left[\int_0^{\lambda_1} \varepsilon_1 L d\lambda + \int_{\lambda_1}^{\lambda_2} \varepsilon(\lambda) L d\lambda + \int_{\lambda_2}^\infty \varepsilon_2 L d\lambda \right] \quad (27)$$

where $\sigma T^4/\pi$ is the total normal radiance emitted by a blackbody and the $\varepsilon^{(i)}$ are random variables described by uniform probability density functions (PDFs) for each side of the spectrum. In the particular case of metals, this becomes:

$$f(\varepsilon_i) = \begin{cases} U(\varepsilon_{max}, 1) & \text{for } \varepsilon_1 \\ U(0, \varepsilon_{min}) & \text{for } \varepsilon_2 \end{cases} \quad (28)$$

where $U(a, b)$ stands for the uniform distribution.

The final equation then becomes:

$$\varepsilon_T = \varepsilon_1 F_{0 \rightarrow \lambda_1}(T) + \varepsilon_2 F_{\lambda_2 \rightarrow \infty}(T) + \frac{\pi}{\sigma T^4} \int_{\lambda_1}^{\lambda_2} \varepsilon_\lambda L_\lambda d\lambda \quad (29)$$

where ε_1 and ε_2 are uniform PDFs given by Eq. 28, λ_1 and λ_2 are the shortest and the longest wavelength of the experimental spectral interval, and $F_{a \rightarrow b}(T)$ stands for the fraction of the total radiance emitted by a blackbody in the $a - b$ wavelength range at temperature T . This function can be computed by numerical integration, series expansion [45], or analytic solutions based on polylogarithmic functions [60]. An illustration of this method is shown in Fig. 11 for normal spectral data of Ni at 673 K.

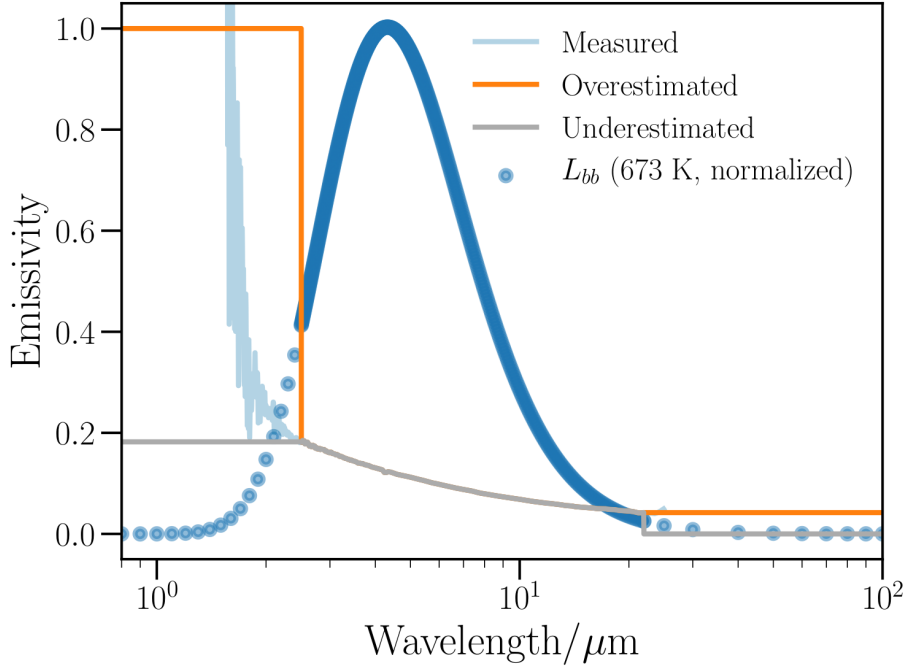


Figure 11: Graphic representation of the extrapolation procedure for Ni using normal spectral data from Fig 4. Emissivity curves are shown as solid lines, corresponding to measured data (shaded blue), the overestimated limits (solid orange) and the underestimated ones (solid grey). A normalized blackbody radiation spectrum (blue dots) is shown to illustrate the relative weight of each spectral region.

Eq. 27 and Eq. 29 are based on the least-informative PDF given the only information that the emissivity in the chosen material is monotonic (as recommended by GUM in the case of lack of information). This is guaranteed in the particular case of metals due to the Drude law holding qualitatively for most of the range up to the visible range [45], but can be easily generalizable to any material with a known monotonic emissivity. Other types of extrapolations, such as assuming a constant emissivity value, are possible [58]. Furthermore, since the weight of the Planck function decreases exponentially away from the Wien peak, the emissivity is only required to be monotonic for the spectral range in

which the Planck function is non-negligible.

In the case of angular integration to obtain the total hemispherical emissivity (Eq. 26), the extrapolations are much simpler. The emissivity values at the extremes are given by the electromagnetic theory as $\varepsilon(0^\circ) \simeq \varepsilon(10^\circ)$ and $\varepsilon(90^\circ) = 0$ [45]. This makes the calculation of the total hemispherical emissivity a simple generalization of the total normal one and with an uncertainty almost equal to those of the individual total directional emissivities.

5.2. Propagation of uncertainties by a Monte Carlo method

The complexity of Eq. 29 makes the standard approach of propagation of uncertainties from spectral data to the total data difficult. In particular, the presence of an integral and the multiple instances of non-linear temperature dependence are the most demanding tasks. Therefore, the standard linearized approach to calculate the uncertainties is discouraged. A Monte Carlo method has been applied following the guidelines of the Supplement 1 to the GUM [37]. The propagation of uncertainties using Monte Carlo methods is common for complex models involving numerical integrals in the field of radiometry [61, 62]. This approach is more general and less biased than the conventional method because it propagates the entire distribution functions describing each of the variables.

Table 3: Uncertainty sources for the calculation of the total emissivities and their distributions.

Source	Symbol	Distribution
Sample temperature	T	Gaussian
Measured emissivities	$\varepsilon(\lambda_i)$	Multivariate Gaussian
Extrapolated emissivities	$\varepsilon_1, \varepsilon_2$	Rectangular

The Monte Carlo method of propagation of uncertainties requires defining the input PDFs for each of the variables that feature in Eq. 29 (T , ε_1 , ε_2 , and each of the $\varepsilon(\lambda_i)$ datapoints). The sample temperature is modelled as Gaussian, as it arises from a combination of uncertainty sources (Eq. 23). The extrapolated emissivities are defined as rectangular PDFs (following Eq. 28), whereas the discrete spectral emissivity data points are drawn from a multivariate Gaussian distribution and assumed to be perfectly correlated ($r = 1$). Quantification of the actual correlation is complicated, but assuming a perfect correlation gives the highest possible uncertainty, whereas assuming no correlation gives an unrealistically low uncertainty value. Therefore, $r = 1$ for all $\varepsilon(\lambda_i)$ is regarded as a conservative but realistic estimate. This approach is similar to that followed in Ref. [44] for the same type of calculation, but without a Monte Carlo approach. It calculates the difference between the maximum possible value within the standard uncertainty and the best estimate of the total emissivity, and assigns it as the standard uncertainty of this parameter. This estimation relies implicitly on an assumption of perfect correlation between all data points. In any case, a full Monte Carlo analysis is deemed more robust because of the complexity of Eq. 29. In particular, the GUM Supplement warns of significant errors in the determination of both the mean and the standard uncertainty when performing these calculations for heavily non-linear functions [37].

In this work, a Monte Carlo method has been implemented in Python 3.7 on a computer running Windows 10. Standard functions from the NumPy (v1.16.4)

and SciPy (v1.3.0) libraries have been used. The pseudo-random generator used has been the standard Mersenne Twister (MT19937) implemented in that version of NumPy. Parallelization issues have been avoided by running the program serially [61]. Two different sets with numbers of trials of $M = 100$ and $M = 32000$ have been calculated from an initial high-entropy seed, while different seed values have also been tried to check the independence of the results from numerical biases. The latter number of trials has been selected as appropriate for a 68% confidence interval (coverage factor $k = 1$), according to the recommendations of Ref. [37], whereas the former has been used as a check to verify that the mean and standard deviation of the result are stable and do not evolve significantly with the number of trials. Other sample statistics may require a larger number of trials.

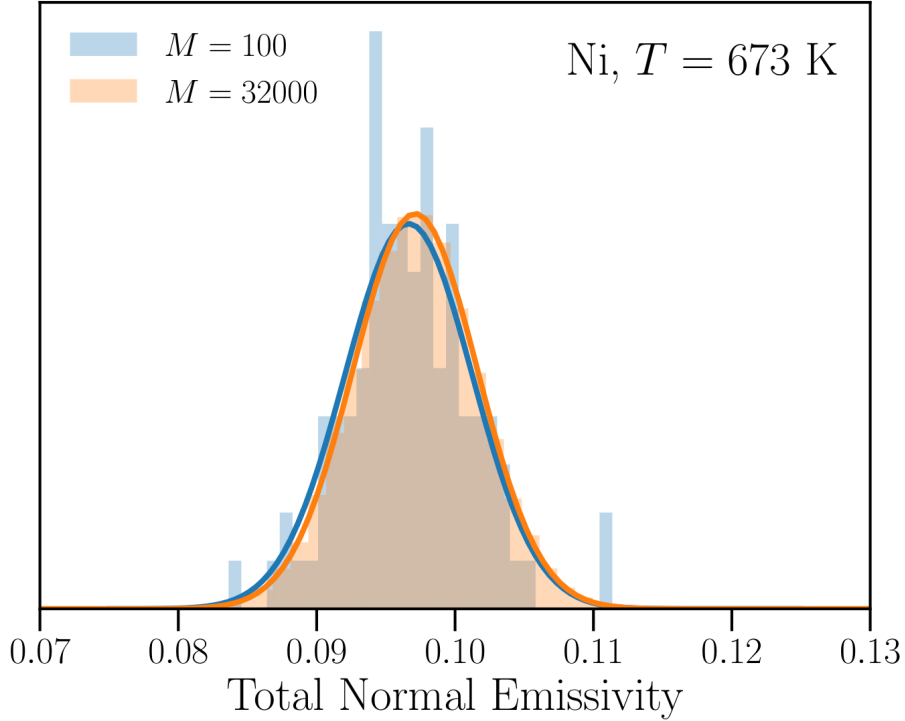


Figure 12: Calculation of the total normal emissivity of Ni at 673 K and its standard uncertainty ($k = 1$) by a Monte Carlo method using two different numbers of trials ($M = 100$ and $M = 32000$). Solid lines correspond to Gaussian fittings to the histograms.

The resulting PDFs from the calculations in are shown in Fig. 12 for one temperature, together with Gaussian fittings to the data. It can be seen that both means and standard deviations agree satisfactorily, even though the histograms are very different. The results of these calculations for all temperatures are shown in Fig. 13. Literature data from Ref. [63], obtained with a similar radiometric method, is shown for comparison. It can be seen that the results obtained in this work compare favourably to those reported in the literature in a semi-quantitative manner, although a clear offset is appreciable. Possible reasons for the discrepancy may involve either differences in sample purity or

surface state or some systematic source that is different in both setups. Further work needs to be done in this regard.

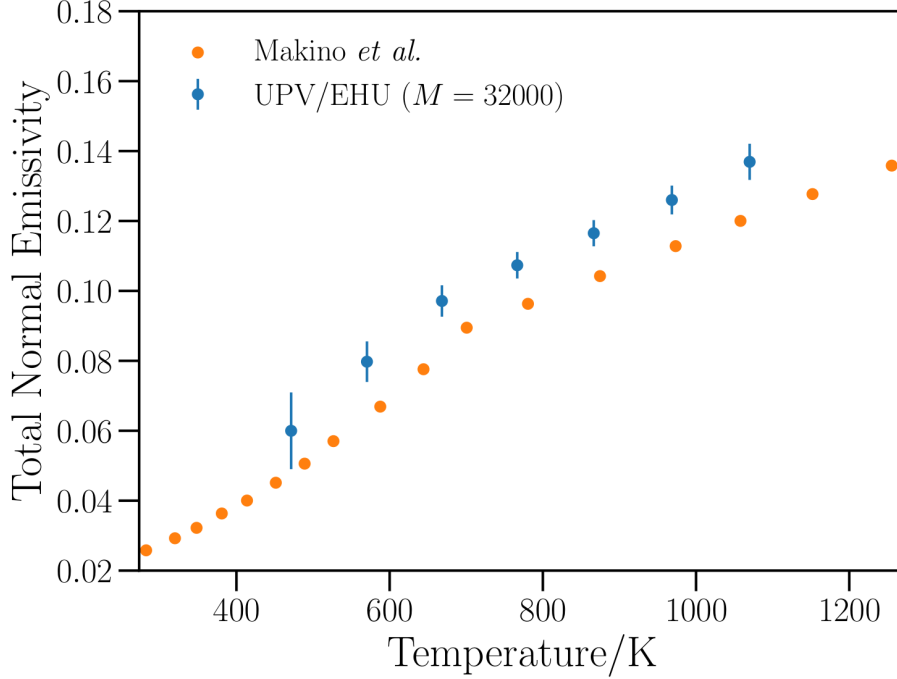


Figure 13: Total normal emissivity and its standard uncertainty ($k = 1$) of Ni calculated using the Monte Carlo method for $M = 32000$. Literature data from Ref. [63] are shown for comparison.

In order to illustrate this approach also for the integration of directional data, results corresponding to a recently published study on V-4Cr-4Ti alloys have been used [38]. These materials are regarded as candidate structural materials for nuclear fusion reactors, and so their total radiative power is of key interest. Directional spectral data are integrated to yield the total directional emissivities and the total hemispherical one. Fig. 14 shows the total directional emissivities with their uncertainties and the calculated total hemispherical emissivity. A multivariate Gaussian distribution with complete correlation ($r = 1$) has been assumed again as a conservative estimate. The resulting value for the total hemispherical emissivity is thus $\varepsilon_H = 0.151 \pm 0.007$, which agrees within two standard uncertainties with the value of 0.136 predicted by the free-electron theory from electrical resistivity data, as reported in Ref. [38]. The results are higher than the prediction, which is somewhat expected given the non-ideal nature of the measured surface [45]. It should also be noted that the theoretical estimate also relies on the quality of the electrical resistivity data used, for which no reported uncertainty or detailed microstructure are available.

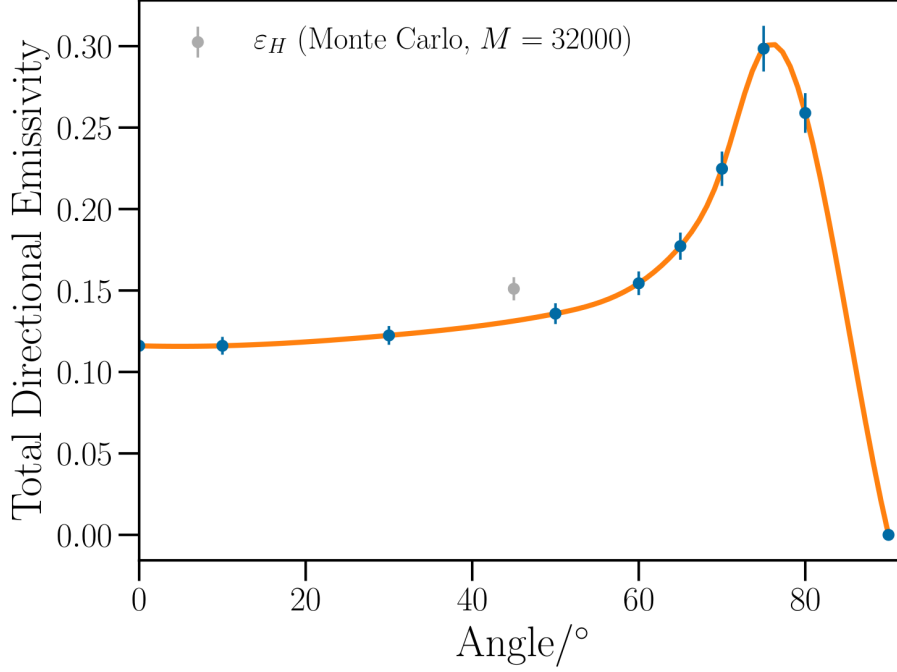


Figure 14: Total emissivities and combined uncertainties of V-4Cr-4Ti at 673 K (blue dots), and total hemispherical emissivity computed using a Monte Carlo method (grey dot). The orange solid line is a calculated spline which is used for the integration of the data.

6. Conclusions

Emissivity measurements are complex procedures that require robust experimental methods. This work details an update of the framework followed at the UPV/EHU for the emissivity measurements performed with the HAIRL radiometer, with particular emphasis in the experimental and methodological improvements.

Concerning the former, the temperature and vacuum ranges have been broadened significantly. In addition, the use of an integrating sphere contributes with valuable room-temperature indirect complementary data. With respect to the latter, there are three main modifications applied to the measurement equation. First, the inclusion of optical path anisotropies and reference emissivities; second, the reformulation of the measurement equation to avoid correlation between the calibration parameters; and third, the addition of different temperature measurement methods for metals and ceramics. Furthermore, a systematic review of the uncertainty budget following the ISO GUM guidelines has been applied to the spectral data. Finally, an integration and extrapolation procedure for calculation of total emissivities, and their uncertainty calculations using a Monte Carlo method are also reported.

This framework has been applied successfully to metallic and ceramic materials, and is expected to be very useful to current and future development of similar emissivity-measuring devices.

Acknowledgements

I. González de Arrieta acknowledges the Basque Government for its support through a PhD fellowship.

References

- [1] E. Le Baron, O. Raccurt, P. Giraud, M. Adier, J. Barriga, B. Diaz, P. Echegut, D. De Sousa Meneses, C. Capiani, D. Sciti, A. Soum-Glaude, C. Escape, I. Jerman, G. A. López, T. Echániz, M. J. Tello, F. Matino, A. Maccari, L. Mercatelli, E. Sani, Round robin test for the comparison of spectral emittance measurement apparatuses, *Solar Energy Materials and Solar Cells* 191 (2019) 476 – 485. doi:10.1016/j.solmat.2018.11.026.
- [2] D. Cárdenas-García, C. Monte, Bilateral intercomparison of spectral directional emissivity measurement between CENAM and PTB, *International Journal of Thermophysics* 35 (2014) 1299–1309. doi:10.1007/s10765-014-1686-1.
- [3] J. Redgrove, M. Battuello, An intercomparison of normal spectral emissivity measurements between NPL (UK) and IMGC (Italy), *High Temperatures-High Pressures* 27-28 (1995) 135–146. doi:10.1068/htrt72.
- [4] L. Hanssen, B. Wilthan, J. R. Filtz, J. Hameury, F. Girard, M. Battuello, J. Ishii, J. Hollandt, C. Monte, Infrared spectral normal emittance/emissivity comparison, *Metrologia* 53 (2016) 03001. doi:10.1088/0026-1394/53/1A/03001.
- [5] J.-R. Filtz, J. Hameury, Intercomparison of total hemispherical and normal spectral emissivity measurements, Tech. rep., EURAMET report (2000). URL https://www.euramet.org/Media/docs/projects/516_THERM_Final.pdf
- [6] Standard practice for calculating solar reflectance index of horizontal and low-sloped opaque surfaces, Standard, ASTM International, West Conshohocken, PA (2001). doi:10.1520/E1980-11.
- [7] Standard practice for measuring and compensating for emissivity using infrared imaging radiometers, Standard, ASTM International, West Conshohocken, PA (2014). doi:10.1520/E1933-14.
- [8] Standard test method for determination of emittance of materials near room temperature using portable emissometers, Standard, ASTM International, West Conshohocken, PA (2015). doi:10.1520/C1371-15.
- [9] Standard guide for testing the thermal properties of advanced ceramics, Standard, ASTM International, West Conshohocken, PA (2013). doi:10.1520/C1470-06R13.
- [10] Standard test methods for total normal emittance of surfaces using inspection-meter techniques, Standard, ASTM International, West Conshohocken, PA (2013). doi:10.1520/E0408-13.

- [11] Standard test method for total hemispherical emittance of surfaces up to 1400 °C, Standard, ASTM International, West Conshohocken, PA (2013). doi:10.1520/C0835-06R13E01.
- [12] S. Rudtsch, H. P. Ebert, F. Hemberger, G. Barth, R. Brandt, U. Groß, W. Hohenauer, K. Jaenicke-Roessler, E. Kaschnitz, E. Pfaff, W. Pöbnecker, G. Pottlacher, M. Rhode, B. Wilthan, Intercomparison of thermophysical property measurements on an austenitic stainless steel, *International Journal of Thermophysics* 26 (2005) 855–867. doi:10.1007/s10765-005-5582-6.
- [13] F. Pavese, About the treatment of systematic effects in metrology, *Measurement* 42 (10) (2009) 1459 – 1462. doi:10.1016/j.measurement.2009.07.017.
- [14] J.-R. Filtz, J. Wu, C. Stacey, J. Hollandt, C. Monte, B. Hay, J. Hameury, M. A. Villamañan, E. Thurzo-Andras, S. Sarge, A European roadmap for thermophysical properties metrology, *International Journal of Thermophysics* 36 (2015) 516–528. doi:10.1007/s10765-014-1807-x.
- [15] M. Honner, P. Honnerová, Survey of emissivity measurement by radiometric methods, *Appl. Opt.* 54 (2015) 669–683. doi:10.1364/AO.54.000669.
- [16] Y. M. Guo, S. J. Pang, Z. J. Luo, Y. Shuai, H. P. Tan, H. Qi, Measurement of directional spectral emissivity at high temperatures, *International Journal of Thermophysics* 40 (1) (2018) 10. doi:10.1007/s10765-018-2472-2.
- [17] K. Zhang, K. Yu, Y. Liu, Y. Zhao, An improved algorithm for spectral emissivity measurements at low temperatures based on the multi-temperature calibration method, *Int. J. Heat Mass Tran.* 114 (2017) 1037 – 1044. doi:10.1016/j.ijheatmasstransfer.2017.06.133.
- [18] K. Zhang, Y. Zhao, K. Yu, Y. Liu, Development of experimental apparatus for precise emissivity determination based on the improved method compensating disturbances by background radiation, *Infrared Physics & Technology* 92 (2018) 350 – 357. doi:10.1016/j.infrared.2018.06.031.
- [19] A. Adibekyan, C. Monte, M. Kehrt, B. Gutschwager, J. Hollandt, Emissivity measurement under vacuum from 4 μm to 100 μm and from -40 °C to 450 °C at PTB, *International Journal of Thermophysics* 36 (2015) 283–289. doi:10.1007/s10765-014-1745-7.
- [20] S. Krenek, D. Gilbers, K. Anhalt, D. R. Taubert, J. Hollandt, A dynamic method to measure emissivity at high temperatures, *International Journal of Thermophysics* 36 (8) (2015) 1713–1725. doi:10.1007/s10765-015-1866-7.
- [21] D. Urban, S. Krenek, K. Anhalt, D. R. Taubert, Improving the dynamic emissivity measurement above 1000 K by extending the spectral range, *International Journal of Thermophysics* 39 (1) (2017) 10. doi:10.1007/s10765-017-2339-y.

- [22] Y. Zhang, G. Diebold, Photothermal determination of the angular dependence of emissivity, *Appl. Opt.* 57 (22) (2018) 6561–6564. doi:10.1364/AO.57.006561.
- [23] Y. Zhang, G. J. Diebold, Emissivity determination using the photoacoustic effect, *Appl. Opt.* 57 (11) (2018) 2790–2794. doi:10.1364/AO.57.002790.
- [24] A. Adibekyan, E. Kononogova, C. Monte, J. Hollandt, Review of PTB measurements on emissivity, reflectivity and transmissivity of semitransparent fiber-reinforced plastic composites, *International Journal of Thermophysics* 40 (4) (2019) 36. doi:10.1007/s10765-019-2498-0.
- [25] F. Zhang, K. Yu, K. Zhang, Y. Liu, K. Xu, Y. Liu, An emissivity measurement apparatus for near infrared spectrum, *Infrared Physics & Technology* 73 (2015) 275 – 280. doi:10.1016/j.infrared.2015.10.001.
- [26] J. Ma, Y. Zhang, L. Wu, H. Li, L. Song, An apparatus for spectral emissivity measurements of thermal control materials at low temperatures, *Materials* 12 (7) (2019) 1141. doi:10.3390/ma12071141.
- [27] B. Kong, T. Li, Q. Eri, Normal spectral emissivity of GH536 (HastelloyX) in three surface conditions, *Applied Thermal Engineering* 113 (2017) 20 – 26. doi:10.1016/j.applthermaleng.2016.11.022.
- [28] D. De Sousa Meneses, P. Melin, L. del Campo, L. Cosson, P. Echegut, Apparatus for measuring the emittance of materials from far infrared to visible wavelengths in extreme conditions of temperature, *Infrared Physics & Technology* 69 (2015) 96 – 101. doi:10.1016/j.infrared.2015.01.011.
- [29] P. Giraud, J. Braillon, O. Raccurt, Selective solar absorber emittance measurement at elevated temperature, *AIP Conference Proceedings* 1850 (1) (2017) 130004. doi:10.1063/1.4984498.
- [30] L. del Campo, R. B. Pérez-Sáez, X. Esquisabel, I. Fernández, M. J. Tello, New experimental device for infrared spectral directional emissivity measurements in a controlled environment, *Review of Scientific Instruments* 77 (2006) 113111. doi:10.1063/1.2393157.
- [31] J. Ishii, A. Ono, Uncertainty estimation for emissivity measurements near room temperature with a Fourier transform spectrometer, *Measurement Science and Technology* 12 (2001) 2103. doi:10.1088/0957-0233/12/12/311.
- [32] S. I. Woods, T. M. Jung, D. R. Sears, J. Yu, Emissivity of silver and stainless steel from 80 K to 300 K: Application to ITER thermal shields, *Cryogenics* 60 (2014) 44 – 48. doi:10.1016/j.cryogenics.2014.01.002.
- [33] J. Hameury, S. Clausen, F. Manoocheri, R. Kersting, J. Manara, T. Meisel, C. Monte, E. Palacio, G. P. Adorno, H. Simon, Improvement of emissivity measurements on reflective insulation materials, in: 20th Symposium on Thermophysical Properties, Boulder, CO, 2018. URL https://thermosymposium.nist.gov/pdf/Abstract_3562.pdf

- [34] Joint Committee for Guides in Metrology (JCGM), Evaluation of measurement data—Guide to the Expression of Uncertainty in Measurement, Tech. Rep. JCGM 100:2008 (2008).
- [35] L. del Campo, R. B. Pérez-Sáez, L. González-Fernández, M. J. Tello, Combined standard uncertainty in direct emissivity measurements, *Journal of Applied Physics* 107 (2010) 113510. doi:10.1063/1.3431541.
- [36] L. del Campo, R. B. Pérez-Sáez, M. J. Tello, X. Esquisabel, I. Fernández, Armco iron normal spectral emissivity measurements, *International Journal of Thermophysics* 27 (2006) 1160–1172. doi:10.1007/s10765-006-0081-y.
- [37] Joint Committee for Guides in Metrology (JCGM), Evaluation of measurement data - Supplement 1 to the Guide to the expression of uncertainty in measurement” - Propagation of distributions using a Monte Carlo method, Tech. Rep. JCGM 101:2008 (2008).
- [38] T. Echániz, I. González de Arrieta, R. Fuente, I. Urcelay-Olabarria, J. M. Igartua, N. de la Pinta, W. Ran, H. Fu, J. Chen, P. F. Zheng, M. J. Tello, G. A. López, Thermal radiative properties of electron-beam-melted and mechanically alloyed V-4Cr-4Ti based alloys between 200 and 750 °C, *Journal of Nuclear Materials* 513 (2019) 86 – 93. doi:10.1016/j.jnucmat.2018.10.051.
- [39] I. González de Arrieta, T. Echániz, R. B. Pérez-Sáez, M. J. Tello, Thermo-radiative and optical properties of a cutting tool based on polycrystalline cubic boron nitride (PCBN), *Materials Research Express* 3 (2016) 045904. doi:10.1088/2053-1591/3/4/045904.
- [40] N. R. Keltner, J. V. Beck, Surface temperature measurement errors, *Journal of Heat Transfer* 105 (2) (1983) 312–318. doi:10.1115/1.3245580.
- [41] R. B. Pérez-Sáez, L. del Campo, M. J. Tello, Analysis of the accuracy of methods for the direct measurement of emissivity, *International Journal of Thermophysics* 29 (2008) 1141–1155. doi:10.1007/s10765-008-0402-4.
- [42] L. González-Fernández, R. B. Pérez-Sáez, L. del Campo, M. J. Tello, Analysis of calibration methods for direct emissivity measurements, *Appl. Opt.* 49 (2010) 2728–2735. doi:10.1364/AO.49.002728.
- [43] T. Echániz, R. B. Pérez-Sáez, M. J. Tello, IR radiometer sensitivity and accuracy improvement by eliminating spurious radiation for emissivity measurements on highly specular samples in the 2 – 25 μm spectral range, *Measurement* 110 (2017) 22 – 26. doi:10.1016/j.measurement.2017.06.010.
- [44] C. Monte, J. Hollandt, The determination of the uncertainties of spectral emissivity measurements in air at the PTB, *Metrologia* 47 (2) (2010) S172–S181. doi:10.1088/0026-1394/47/2/s14.
- [45] J. R. Howell, M. P. Menguc, R. Siegel, Thermal radiation heat transfer, CRC press, 2015.

- [46] D. Cárdenas-García, Emissivity measurement of high-emissivity black paint at CENAM, *Revista Mexicana de Física* 60 (2014) 305–308.
- [47] B. Rousseau, J. F. Brun, D. De Sousa Meneses, P. Echegut, Temperature measurement: Christiansen wavelength and blackbody reference, *International Journal of Thermophysics* 26 (4) (2005) 1277–1286. doi:10.1007/s10765-005-6726-4.
- [48] J. T. Nakos, Uncertainty analysis of thermocouple measurements used in normal and abnormal thermal environment experiments at Sandia’s Radiant Heat Facility and Lurance Canyon Burn Site, Tech. rep., Sandia National Laboratories, SANDIA REPORT SAND2004-1023 (2004). URL <http://prod.sandia.gov/techlib/access-control.cgi/2004/041023.pdf>
- [49] G. Teodorescu, P. D. Jones, Spectral and directional emittance of alumina at 823 K, *Journal of Materials Science* 43 (2008) 7225–7229. doi:10.1007/s10853-008-2945-y.
- [50] A. Mangano, G. Coggiola, Stability of K-, N- and S-type thermocouples in the temperature range from 0 °C to 1060 °C, *Measurement* 12 (1993) 171 – 182. doi:10.1016/0263-2241(93)90024-C.
- [51] T. G. Kollie, J. L. Horton, K. R. Carr, M. B. Herskovitz, C. A. Mossman, Temperature measurement errors with type K (Chromel vs Alumel) thermocouples due to short-ranged ordering in Chromel, *Review of Scientific Instruments* 46 (11) (1975) 1447–1461. doi:10.1063/1.1134086.
- [52] P. Pavlasek, C. J. Elliott, J. V. Pearce, S. Duris, R. Palencar, M. Koval, G. Machin, Hysteresis effects and strain-induced homogeneity effects in base metal thermocouples, *International Journal of Thermophysics* 36 (2015) 467–481. doi:10.1007/s10765-015-1841-3.
- [53] E. S. Webster, Drift in type K bare-wire thermocouples from different manufacturers, *International Journal of Thermophysics* 38 (2017) 70. doi:10.1007/s10765-017-2210-1.
- [54] E. S. Webster, Seebeck changes due to residual cold-work and reversible effects in type K bare-wire thermocouples, *International Journal of Thermophysics* 38 (2017) 135. doi:10.1007/s10765-017-2269-8.
- [55] L. M. Hanssen, C. P. Cagran, A. V. Prokhorov, S. N. Mekhontsev, V. B. Khromchenko, Use of a high-temperature integrating sphere reflectometer for surface-temperature measurements, *International Journal of Thermophysics* 28 (2) (2007) 566–580.
- [56] A. Adibekyan, E. Kononogova, C. Monte, J. Hollandt, High-accuracy emissivity data on the coatings Nextel 811-21, Herberts 1534, Aeroglaze Z306 and Acktar Fractal Black, *International Journal of Thermophysics* 38. doi:10.1007/s10765-017-2212-z.
- [57] I. González de Arrieta, T. Echániz, J. M. Olmos, R. Fuente, I. Urcelay-Olabarria, J. M. Igartua, M. J. Tello, G. A. López, Evolution of the infrared emissivity of Ni during thermal oxidation until oxide layer opacity, *Infrared Physics & Technology* 97 (2019) 270 – 276. doi:10.1016/j.infrared.2019.01.002.

- [58] J.-P. Monchau, J. Hameury, P. Ausset, B. Hay, L. Ibos, Y. Candau, Comparative study of radiometric and calorimetric methods for total hemispherical emissivity measurements, *Heat and Mass Transfer* 54 (2018) 1415–1425. doi:10.1007/s00231-017-2238-6.
- [59] I. Setién-Fernández, T. Echániz, L. González-Fernández, R. B. Pérez-Sáez, E. Céspedes, J. A. Sánchez-García, L. Álvarez-Fraga, R. E. Galindo, J. M. Albella, C. Prieto, M. J. Tello, First spectral emissivity study of a solar selective coating in the 150 – 600 °C temperature range, *Solar Energy Materials and Solar Cells* 117 (2013) 390 – 395. doi:10.1016/j.solmat.2013.07.002.
- [60] S. M. Stewart, Blackbody radiation functions and polylogarithms, *Journal of Quantitative Spectroscopy and Radiative Transfer* 113 (2012) 232 – 238. doi:10.1016/j.jqsrt.2011.10.010.
- [61] T. J. Esward, A. de Ginestous, P. M. Harris, I. D. Hill, S. G. R. Salim, I. M. Smith, B. A. Wichmann, R. Winkler, E. R. Williams, A Monte Carlo method for uncertainty evaluation implemented on a distributed computing system, *Metrologia* 44 (5) (2007) 319–326. doi:10.1088/0026-1394/44/5/008.
- [62] R. R. Cordero, G. Seckmeyer, D. Pissulla, F. Labbe, Uncertainty of experimental integrals: application to the UV index calculation, *Metrologia* 45 (1) (2007) 1–10. doi:10.1088/0026-1394/45/1/001.
- [63] T. Makino, H. Kawasaki, T. Kunitomo, Study of the radiative properties of heat resisting metals and alloys: (1st report, optical constants and emissivities of nickel, cobalt and chromium), *B. JSME* 25 (203) (1982) 804–811. doi:10.1299/jsme1958.25.804.